

Morphological analysis of the cm-wave continuum in the dark cloud LDN 1622

S. Casassus¹, G. Cabrera, F. Förster²

Departamento de Astronomía, Universidad de Chile, Santiago, Casilla 36-D, Chile

T.J. Pearson, A.C.S. Readhead, C. Dickinson

Owens Valley Radio Observatory, California Institute of Technology, Pasadena, CA 91125

simon@das.uchile.cl

ABSTRACT

The spectral energy distribution of the dark cloud LDN 1622, as measured by Finkbeiner using *WMAP* data, drops above 30 GHz and is suggestive of a Boltzmann cutoff in grain rotation frequencies, characteristic of spinning dust emission.

LDN 1622 is conspicuous in the 31 GHz image we obtained with the Cosmic Background Imager, which is the first cm-wave resolved image of a dark cloud. The 31 GHz emission follows the emission traced by the four *IRAS* bands. The normalised cross-correlation of the 31 GHz image with the *IRAS* images is higher by 6.6σ for the 12 μm and 25 μm bands than for the 60 μm and 100 μm bands: $C_{12+25} = 0.76 \pm 0.02$ and $C_{60+100} = 0.64 \pm 0.01$.

The mid-IR – cm-wave correlation in LDN 1622 is evidence for very small grain (VSG) or continuum emission at 26–36 GHz from a hot molecular phase. In dark clouds and their photon-dominated regions (PDRs) the 12 μm and 25 μm emission is attributed to stochastic heating of the VSGs. The mid-IR and cm-wave dust emissions arise in a limb-brightened shell coincident with the PDR of LDN 1622, where the incident UV radiation from the Ori OB 1b association heats and charges the grains, as required for spinning dust.

Subject headings: radio continuum: ISM, radiation mechanisms: general, infrared: ISM, ISM: dust, ISM: clouds

¹email address: simon@das.uchile.cl

²Denys Wilkinson building, Physics Department, Oxford University, Keble Road, Oxford OX1 3RH

1. Introduction

An increasing amount of evidence supports the existence of a new continuum emission mechanism in the diffuse interstellar medium (ISM) at 10–30 GHz, other than free-free, synchrotron, or an hypothetical Rayleigh-Jeans tail of cold dust grains¹ (Leitch et al. 1997; de Oliveira-Costa et al. 1999; Finkbeiner et al. 1999; de Oliveira-Costa et al. 2002; Lagache 2003; Banday et al. 2003; Finkbeiner 2004). Examples of excess emission at cm-wavelengths over known emission mechanisms have been found in the spectral energy distributions (SEDs) of the dark cloud LDN 1622 and the diffuse H II region LPH 201.7+1.6 (Finkbeiner et al. 2002; Finkbeiner 2004), in the Helix planetary nebula (Casassus et al. 2004), and in another diffuse H II region in Perseus (Watson et al. 2005). At the date of writing, the only morphological evidence for the existence of a new emission mechanism at cm-wavelengths in a specific object is provided by the Helix nebula. But a comparative analysis of the cm-wave, mid- and far-IR continua in the Helix is hampered by strong line contamination in the short wavelength *IRAS* maps. The Cosmic Background Imager (CBI) observations of LDN 1622 provide an opportunity of performing such morphological analysis.

As modelled by Draine & Lazarian (1998a,b) a possible candidate mechanism is electric dipole emission from spinning very small grains (VSGs), or ‘spinning dust’. The spectral energy distribution of the dark cloud LDN 1622 (Lynds Dark Nebula, Lynds 1962) is suggestive of spinning dust: it rises over 5–9.75 GHz (Finkbeiner et al. 2002), following dipole emission, and then drops above 30 GHz (Finkbeiner 2004), as expected from a Boltzmann cutoff in the grain rotation frequencies.

The dark cloud LDN 1622 lies within the Orion East molecular cloud (Maddalena et al. 1986), at a distance of ~ 120 pc (Wilson et al. 2005) and in the foreground of the Orion B cloud. Its far-IR linear size is slightly less than 1 pc. It is a conspicuous CS(2–1) and N₂H⁺ “starless”² core (Lee et al. 2001, with an H₂ density of $\sim 10^3 - 10^4$ cm⁻³). LDN 1622 is devoid of H II regions, aside from Barnard’s Loop (e.g. Boumis et al. 2001), a very diffuse H II region (Heiles et al. 2000, with electron density of 2 cm⁻³) separated by ~ 1 deg from LDN 1622. No free-free emission is expected from LDN 1622, which is indeed absent from the Parkes-MIT-NRAO survey at 5 GHz³ (hereafter PMN survey, Condon et al. 1993, as presented in

¹such traditional grain emission is that due to thermal oscillations of the grain charge distribution (e.g. Draine & Lazarian 1999)

²LDN 1622 does contain entries in the *IRAS* Point Source Catalog, and probably hosts low-mass young stellar objects, see Appendix C

³Given that the 1σ noise level in the PMN survey is 5 mJy beam⁻¹, the free-free emission measure towards LDN 1622 must be less than 10 pc cm⁻⁶, which for a spherical nebula 10 arcmin in diameter implies

SkyView, <http://skyview.gsfc.nasa.gov>). Only the H α corona of LDN 1622, outlining its photon-dominated region, is marginally detected in the PMN survey.

Here we present the first cm-wave continuum image of a dark cloud, and report morphological evidence that supports spinning dust as the mechanism responsible for the anomalous foreground. We first describe data acquisition (Section 2), and image reconstruction (Sec. 3), and then discuss the effects of ground spill over and give flux estimates (Sec. 4). We analyse the 31 GHz data by comparison with the *IRAS* bands used as templates for the emission by cool dust and by VSGs (or hot dust, Sec. 5), which leads us to infer a limb-brightened morphology of LDN 1622 at 31 GHz. The comparison with H α and 5 GHz templates shows that any free-free contribution at 31 GHz is negligible, and that the 31 GHz emission is interior to the H α corona of the cloud (Sec. 6). We discuss the spectral energy distribution of LDN 1622 (Sec. 7), and finally summarise our results (Sec. 8).

2. CBI observations

The CBI (Padin et al. 2002) is a planar interferometer array with 13 antennas, each 0.9 m in diameter, mounted on a 6 m tracking platform, which rotates in parallactic angle to provide uniform uv -coverage. The CBI receivers operate in 10 frequency channels, with 1 GHz bandwidth each, giving a total bandwidth of 26–36 GHz. It is located in Llano de Chajnantor, Atacama, Chile.

We observed LDN 1622 (J2000 RA: 05:54:23.0, Dec: +01:46:54) on 03-Nov-2003, 02-Dec-2003 and 21-Nov-2004, for a total 10000 s. The compact configuration of the CBI interferometer results in the (u, v) coverage shown on Fig. 1, where it can be seen that baseline length varies between 100λ and 400λ , corresponding to spatial scales of 34.4 arcmin and 8.6 arcmin, respectively. Each receiver is equipped with phase shifters which allow selecting its polarization mode. We set all receivers to L polarization, so that the visibilities are sensitive to the combination of Stokes parameters $I - V$. In what follows we assume that Stokes V (circular polarization) is negligible in LDN 1622.

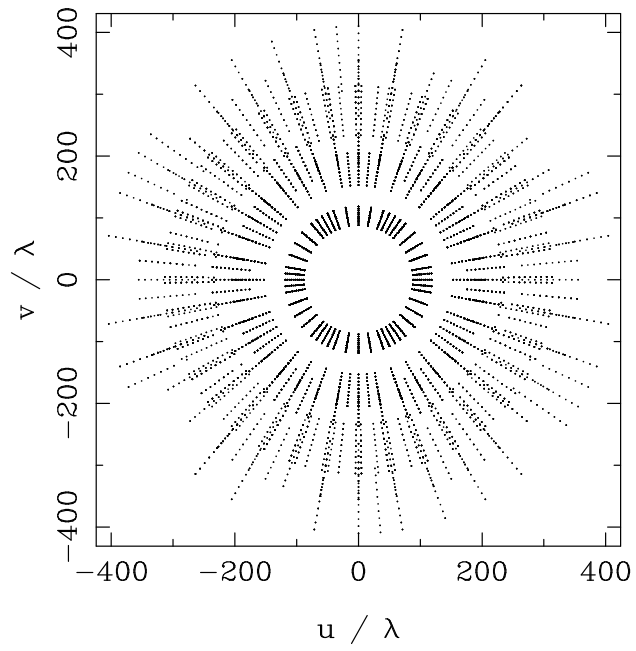


Fig. 1.— (u, v) coverage of the CBI in the compact configuration used for the observations of LDN 1622.

Approximate cancellation of ground and Moon contamination was obtained by differencing with a reference field at the same declination but offset in hour angle by the duration of the on-source integration. We used an on-source integration time of 8 min, with a trailing reference field. For phase calibration purposes we interspersed a 2 min integration on J0607–085 between each 16 min cycle of differenced observations. J0607–085 was observed with identical telescope settings as LDN 1622.

The data were reduced and edited using a special-purpose package (CBICAL, developed by T.J. Pearson). Flux calibration was performed using either Saturn or Tau A, whose fluxes are in turn calibrated against Jupiter (with a temperature of 146.6 K, Page et al. 2003). The flux calibrator is also used as the reference for an initial phase calibration. The phase calibration was subsequently refined by using the calibrator interspersed between each cycle on LDN 1622. We applied a phase shift to bring J0607–085 to the phase center. The magnitude of the offsets by which we had to correct the position of J0607–085 varied between 15 and 40 arcsec.

In a final stage we combined all available visibilities of LDN 1622 to produce two final datasets, with and without reference field subtraction. Since the angular distance of LDN 1622 from the Moon was larger than 80 deg for all three nights of observations, the contamination on the shorter baselines is probably entirely due to ground spill over.

3. Image reconstruction

Image reconstruction is difficult for an object such as LDN 1622, which extends to about half the CBI’s primary beam of 45 arcmin FWHM, and is surrounded by diffuse emission. Additionally the CBI’s synthesized beam obtained with natural weights, ~ 8 arcmin FWHM, is about the size of the object, ~ 10 arcmin. Thus in order to perform a morphological analysis we need to extract a finer resolution from the visibilities than that obtained from the restored images. The maximum entropy method (MEM) fits model images to visibility data. The MEM models can potentially recover details on finer angular scales than the synthesized beam. In this Section we present the results of our reconstructions. The algorithm and model validation are described in Appendices A and B

In Figure 2a we present a MEM model of our data. The noise of the restored image in Fig. 2b is close to that expected from the instrumental noise. The difmap package (Shepherd 1997) estimates a theoretical noise in the dirty map (using natural weights) of 3.2 mJy/beam, which should give 3 σ deviations of about 10 mJy beam⁻¹ for an optimal reconstruction. The dirty map of the residual visibilities, obtained with difmap using natural weights, has a

minimum of -11 mJy/beam within the half-power contour of the primary beam, consistent with the theoretical noise⁴.

⁴the minimum value in the residual image is in fact -24 mJy beam⁻¹, at J2000 equatorial coordinates (89.15 deg,+2.10 deg), which we identify as a 170 mJy point source (PMN J0604+0205) offset by 38 arcmin from the phase center in the reference field. This negative point source in the restored image is at ~ 0.5 deg from the phase centre, and is outside the region of interest

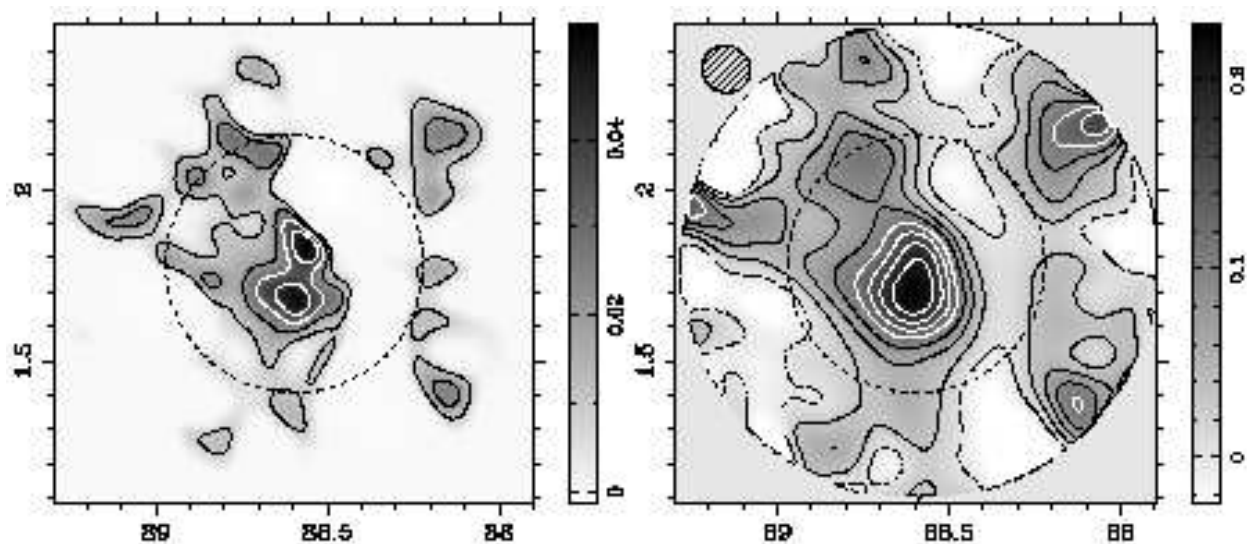


Fig. 2.— Left: MEM model of the CBI data, specific intensity units are MJy sr^{-1} , and contour levels are at $[0.010, 0.020, 0.031, 0.042]$. Right: restored imaged obtained by convolving the MEM model with a gaussian PSF and adding the dirty map of the residual visibilities, specific intensity units are Jy beam^{-1} . The contour levels are at $[0, 0.029, 0.057, 0.086, 0.115, 0.144, 0.172, 0.201]$. Both the PSF ($8.43 \text{ arcmin} \times 8.11 \text{ arcmin}$) and the natural-weight residual image were calculated with difmap. The half-power contour of the primary beam is shown as a dashed circle on both plots.

We also obtained “clean” images with difmap, which qualitatively confirm the MEM models. We show an overlay of the MEM model on a “clean” restoration in Fig. 3a, obtained with the difmap package and uniform weights. We anticipate from Sec. 5 the good match between 31 GHz and 12 μm emission to test which of the two reconstructions, whether MEM or “clean”, extracts the most of the data. Fig. 3b also shows an overlay of the 31 GHz contours on the *IRAS* 12 μm map in grey scale. The *IRAS* 12 μm image is from the *IRAS* Sky Survey Atlas (Wheelock et al. 1991), as obtained in *SkyView*. It can be appreciated by inspection of Fig. 3 that the MEM model recovers low-level details that are absent in the “clean” image, such as the 12 μm emission peaks at (88.8, +2.1) and (88.1, +2.1). There are two features in the MEM model that do not seem to have a 12 μm counterpart. One is a low-level contour at (88.8, +1.3), which turns out to be the location of the brightest radio point source in the field (see Sec. 6 and Fig. 9). The other is a 31 GHz peak at (88.1, +1.4), which matches an $\text{H}\alpha$ feature at the outskirts of Barnard’s Loop (see Fig. 9). We will use MEM in what follows because it provides reconstructions that do not depend on user-defined “clean” boxes, and because it allows extracting details on fine angular scales while preserving the sensitivity of the dataset⁵.

⁵the MEM algorithm implemented here does not apply any gridding, so that the visibilities are assigned their statistical weight only. To reach finer angular resolutions, “clean” reconstructions downweight low spatial frequencies, thereby losing sensitivity.

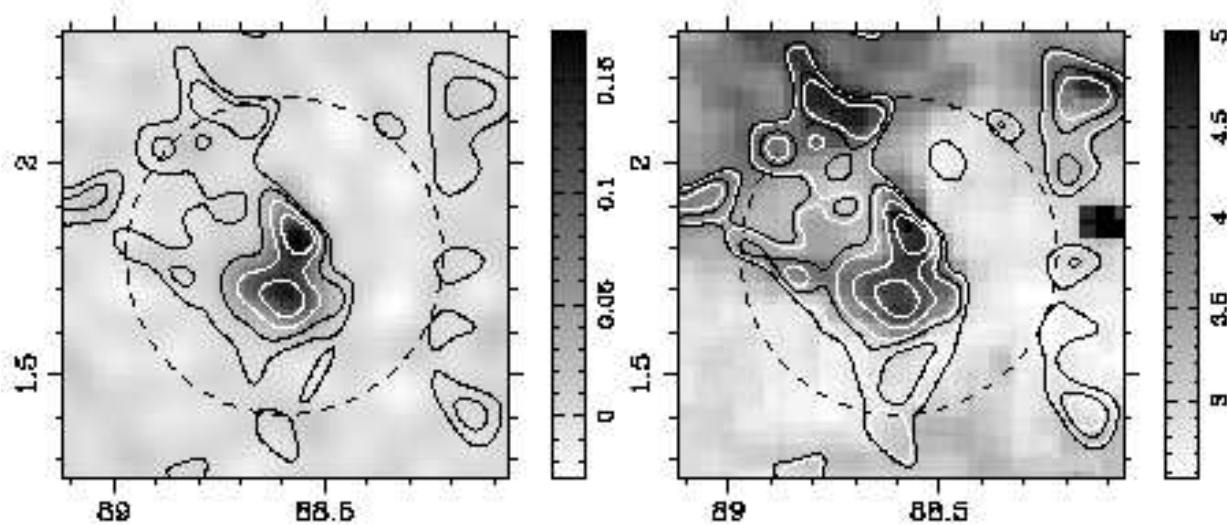


Fig. 3.— left: Overlay of the MEM model (with the same contour levels as in Fig. 2) on a “clean” restoration of the CBI data, obtained with uniform weights in difmap. Units of the grey scale are Jy beam^{-1} , with a $6.14 \times 5.8 \text{ arcmin}^2$ beam (uniform weights). right: Overlay of the MEM model contours on the *IRAS* $12 \mu\text{m}$ map (with the same contours as in Fig. 2, and two extra levels in black, at $[0.008, 0.0168]$). Note the MEM model traces $12 \mu\text{m}$ diffuse emission, but not the $12 \mu\text{m}$ point sources.

The CBI image can be compared with that available in the first *WMAP* data release. Barnard’s loop is the most conspicuous feature in the *WMAP* Ka-band image of the region. But it is apparent that the CBI data on LDN 1622 are much more sensitive, and allow resolving the dark cloud. The CBI image is thus the first at cm-wavelength of a dark nebula, i.e. a cold dust cloud identified by visible-light stellar counts.

4. Ground contamination and average properties of the dataset

In order to cross-correlate the CBI data with the comparison templates we compute template visibilities, obtained by a simulation of CBI observations on the template images (“CBI-simulated visibilities” hereafter, see Appendix A and B). The 31 GHz-100 μm visibility plot on Fig. 4a for the undifferenced dataset allows assessing the level of ground and Moon contamination in the shorter baselines. The enhanced scatter above 100 μm visibilities of $V_{100\mu\text{m}} = 300$ Jy and at $V_{100\mu\text{m}} = \pm 150$ Jy is suppressed in the differenced dataset shown on Fig. 4b.

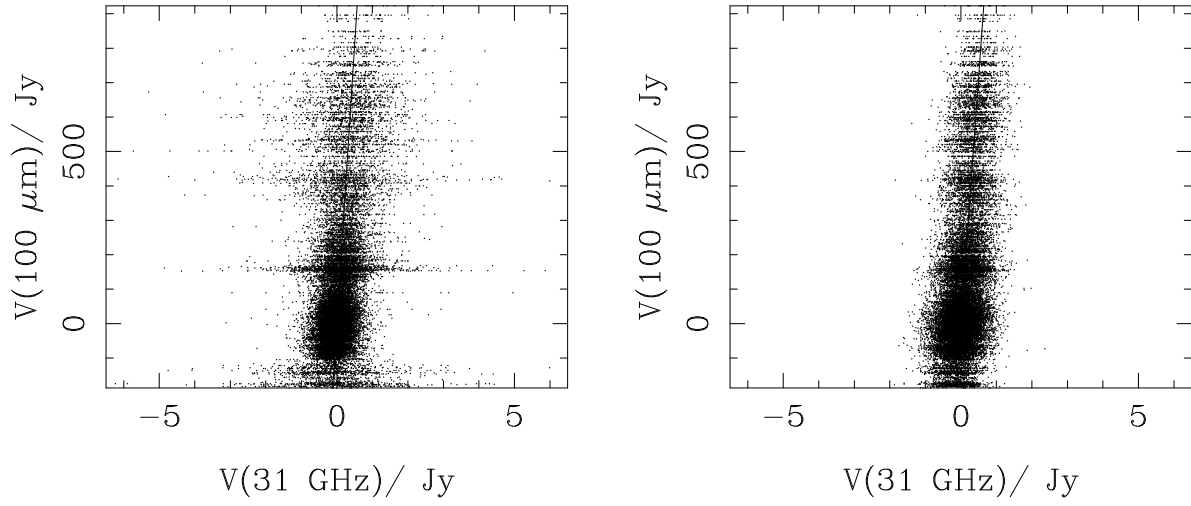


Fig. 4.— 31 GHz-100 μm visibility correlations over the full range of uv -radii, for the non-differenced dataset (left) and for the differenced dataset (right). We plot both the real and imaginary parts.

The enhanced scatter due to ground or Moon contamination in the shorter baselines correspond to where the real parts of $V_{100\mu\text{m}}$ reach about 300 Jy and where the imaginary parts of $V_{100\mu\text{m}}$ reach ± 150 Jy. Restricting to baselines above 120λ retains visibilities devoid of ground contamination, as shown on Fig. 5.

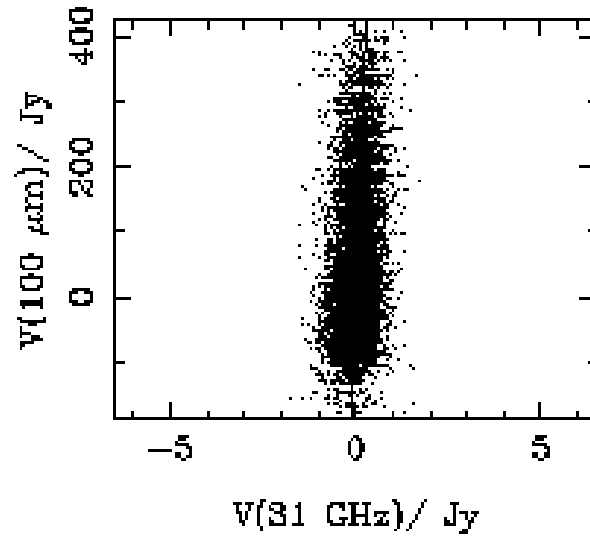


Fig. 5.— 31 GHz-100 μm visibility correlation for the non-differenced dataset and uv -radii $k > 120$.

Typical ISM power spectra are decreasing power-laws (Gautier et al. 1992; Wright 1998; Elmegreen 2002), the ensemble-averaged modulus of the visibility is thus a monotonic function of uv -radius. This is also true for LDN 1622, for the case of the 100 μm CBI-simulated visibilities: the azimuthally averaged power-spectrum is monotonic. We cannot recover a power spectrum for the CBI data by simple averaging because the signal is affected by noise, so that the derived spectrum is artificially flat.

The 31 GHz flux density measured on the restored image within a circular aperture with 45 arcmin diameter centered on LDN 1622 is 1.41 ± 0.03 Jy. We caution that the CBI images are heavily affected by flux loss for emission on 45 arcmin scales: because of incomplete sampling in the uv plane the reconstructed images have missing spatial frequencies, and part of the extended nebular emission is lost. We can infer a flux density corrected for flux loss, of 2.90 ± 0.04 Jy, by referring to a template map, for which we use *IRAS* 100 μm . This flux density is estimated by extracting the flux density in the template map within a 45 arcmin aperture, and scaling by the CBI-*IRAS* 100 μm correlation slope given in Table 1 for the differenced dataset.

Template maps which follow closely the 31 GHz emission also allow a cross-check on the pointing accuracy of the CBI. We vary an (α, δ) shift on the coordinates of the reference pixel of the template maps to minimize $\chi^2 = \|V_i(31 \text{ GHz}) - V_i(\text{IRAS})\|^2 / \sigma_i^2$, where the uncertainties σ_i only contain the CBI noise. The optimal shifts we find for each of the *IRAS* maps are (in arcmin): $(0.66 \pm 0.07, 0.24 \pm 0.08)$, $(0.60 \pm 0.08, 0.14 \pm 0.09)$, $(0.79 \pm 0.08, -0.31 \pm 0.09)$, $(0.08 \pm 0.08, -0.89 \pm 0.09)$ for the 12 μm , 25 μm , 60 μm , and 100 μm maps, respectively. Thus no particular trend is found, although the average values of the shifts is $(+0.5, -0.3)$ arcmin and significantly different from zero. But in what follows we ignore a possible residual error in telescope pointing because the overlays of the 31 GHz and far-IR images in Fig. 6 show a good match, and would not improve by shifting on 0.5 arcmin scales.

5. Comparison with mid- and far-IR templates.

If dust is responsible for the 31 GHz emission in LDN 1622 then a tight relationship is expected with the mid- and far-IR emission. Here we investigate the consequences of assuming that the emission traced by the CBI scales linearly with the four *IRAS* maps.

The infrared emission from dust is discussed in details by, e.g. Désert et al. (1990); Draine & Li (2001); Li & Draine (2001). The *IRAS* 100 μm band traces emission from large grains, with sizes greater than 0.01 μm . The large grains are in equilibrium with the interstellar radiation field, with a temperature of order 10–20 K depending on environment.

Continuum emission at shorter wavelengths is due to hot dust, at ~ 100 K, which is too hot to be maintained in equilibrium with the interstellar UV field. Mid-IR emission from classical hot dust is not expected because of the absence of a strong UV source within LDN 1622, in contrast with compact H II regions or planetary nebulae. Thus stochastic heating of VSGs dominates the dust emission in the *IRAS* $12\mu\text{m}$ and $25\mu\text{m}$ bands. The heat capacity of a VSG is so small that the absorption of a single UV photon increases the particle temperature high enough for it to emit at $< 60\mu\text{m}$.

Thus, by examining the degree of correlation with the 4 *IRAS* bands, we hope to determine which type of grain, whether the large grains or the VSGs, are responsible for the 31 GHz emission. We caution that from the *IRAS* photometry alone we cannot differentiate a 31 GHz link to the VSGs from a link to a hot molecular phase that shines in the H_2 lines. After all the VSGs can also be regarded as large molecules, such as polycyclic aromatic hydrocarbons (PAHs). Another important source of flux in the *IRAS* $12\mu\text{m}$ and $25\mu\text{m}$ bands are the H_2 ro-vibrational lines, such as $\text{H}_2(0-0)\text{S}(2)$ $12.3\mu\text{m}$, and $\text{H}_2(0-0)\text{S}(0)$ $28.2\mu\text{m}$. The H_2 line fluxes integrated over the *IRAS* band passes could account for part of the mid- and far-IR morphological differences (as could be the case in PDRs, with conspicuous H_2 lines, Van Dishoeck 2004).

The 31 GHz MEM contours can be compared by inspection with the raw *IRAS* images, as extracted from *SkyView*. The diffuse emission in the mid-IR images is closer to the 31 GHz contours than the far-IR images. In this section we quantify this qualitative result, and show it is not affected by noise or missing spatial frequencies at 31 GHz.

5.1. Visibility cross-correlations

Is the cm-wave – mid-IR correlation detectable directly in the visibility data? The cross-correlations may be different in the image plane and in the uv plane because of two reasons. One is the contribution of point sources at $12\mu\text{m}$, which are absent at 31 GHz. The fainter point sources at $12\mu\text{m}$ may be numerous and act as diffuse emission⁶. The subtraction of the brightest point sources may not be accurate enough to retain genuinely diffuse emission at $12\mu\text{m}$. Another difficulty with a uv -plane analysis of the diffuse emission are the uncertainties in the CBI primary beam (Pearson et al. 2003, their Fig. 1). Variations between antennas introduce uncertainties beyond about 40 arcmin from the phase center. LDN 1622 is surrounded by diffuse emission, such as that traced by *IRAS*. The outskirts of Barnard’s Loop are within 35 arcmin from the phase center, and it peaks at about 60 arcmin.

⁶see for instance the ISO $6.7\mu\text{m}$ image of LDN 1622 in Fig. 12

Also in the neighborhood of LDN 1622 is the reflection nebula NGC 2067, which at 1.9-2.7 deg from the phase center falls on a sidelobe of the primary beam at 2.2 deg. Barnard’s Loop or NGC 2067 are bound to enter the side lobes and low level wings of the primary beam, where the uncertainties in the primary beam model used in CBI-simulated visibilities become important.

We linearly correlate the CBI visibilities with the CBI-simulated visibilities on the four *IRAS* bands, one template at a time, and after processing as described in Appendix B. Table 1 lists reduced- χ^2 , linear correlation coefficients (as defined in Bevington & Robinson 1992), correlation slopes and uncertainties. In Table 1 we also consider the non-differenced CBI dataset, because its signal to noise ratio (S/N) improves by a factor $\sqrt{2}$. We restrict the analysis of the non-differenced dataset to uv -radii above 120λ . Such a baseline range allows minimizing ground spill over or Moon contamination. Another reason for restricting baseline lengths above a minimum is that a constant background in the template maps affects the simulated visibilities for the shortest baselines. We minimize this effect, which is due to the restricted sky domain available to compute the simulated visibilities, by clipping the templates so that their minimum intensity value is zero.

But from the visibility correlations alone we cannot ascertain which *IRAS* map correlates best with the 31 GHz data. The significance of the results is difficult to assess because the noise in the comparison maps is not known accurately (and is neglected in this analysis), and the confidence level associated to the χ^2 distribution with $\nu \sim 10\,000$ degrees of freedom is extremely sharp at $\chi^2/\nu \approx 1$.

5.2. Image plane cross-correlations

A drawback of analysing the visibility data directly in the Fourier-plane is that the effect of the point sources is difficult to isolate, especially at shorter IR wavelengths, where point sources are more frequent. Here we compare the CBI data and the *IRAS* templates in the image plane, based on our MEM modelling.

5.2.1. Qualitative comparison

Inspection of Fig. 6 reveals that the $12 \mu\text{m}$ and $25 \mu\text{m}$ MEM maps are the most similar to the 31 GHz MEM model. In Fig. 6 the *IRAS* maps are the same as in Fig. 11, i.e. they are reconstructed from simulated CBI visibilities, following the algorithm described in Appendix B. Thus the mid-IR – cm-wave correlation is not the effect of missing spatial

frequencies in the 31 GHz visibility data.

The 100 μm emission is concentrated in a single maximum, while the 31 GHz, 12 μm and 25 μm images show two peaks near the phase center, at the origin of coordinates in Fig. 6, which we refer to as the northern and southern peaks. The 60 μm image is also double-peaked, but the southern peak is offset relative to the 31 GHz southern peak.

The 31 GHz morphology of LDN 1622 is remarkably similar to that in the 12 μm *IRAS* band. However there is an interesting feature at 12 μm which is absent at 31 GHz. The northern peaks at 31 GHz and 12 μm are slightly offset, while the southern peaks are exactly coincident. We explain the shift in the position of the northern peak as being due to a young stellar object (YSO), namely L1622-10, whose emission contributes at 12 μm but not at 31 GHz. Thus the 31 GHz emission is genuinely diffuse, while 12 μm includes photospheric emission, or unresolved very hot dust. The point-source flux for L1622-10, as listed in the *IRAS* Point Source Catalog, is subtracted from the processed *IRAS* 12 μm image used as comparison template (see Appendix B). But the YSO is still present in the processed image, even after subtraction, as can be inferred by comparing the raw *IRAS* 12 μm image in Fig. 3 and the processed image in Fig. 6. The imperfect subtraction of L1622-10 is probably due to an inaccurate catalog flux, perhaps due to the uncertainties inherent in deriving a flux density for a point source on top of a compact source, such as the northern peak. A discussion on the properties of this YSO is given in Appendix C.

Table 1. Linear correlation results

	12 μm	25 μm	60 μm	100 μm
A: differenced dataset, $f = 25724$				
χ^2/f :	1.07	1.06	1.06	1.06
r :	0.395	0.399	0.394	0.395
a :	24.86 ± 0.30	14.86 ± 0.18	2.64 ± 0.03	0.70 ± 0.01
B: non-differenced dataset, $k > 120$, $f = 16016$				
χ^2/f :	1.74	1.74	1.74	1.75
r :	0.243	0.241	0.246	0.242
a :	20.09 ± 0.46	13.09 ± 0.30	2.60 ± 0.06	0.68 ± 0.02

Note. — f is the number of degrees of freedom (which is the number of observed visibilities above a uv -radius k , minus one free-parameter), r is the linear correlation coefficient, and a is the conversion factor between the various templates and the 31 GHz visibilities, such that $V(31 \text{ GHz}) = 10^{-3} a V(\text{IR})$.

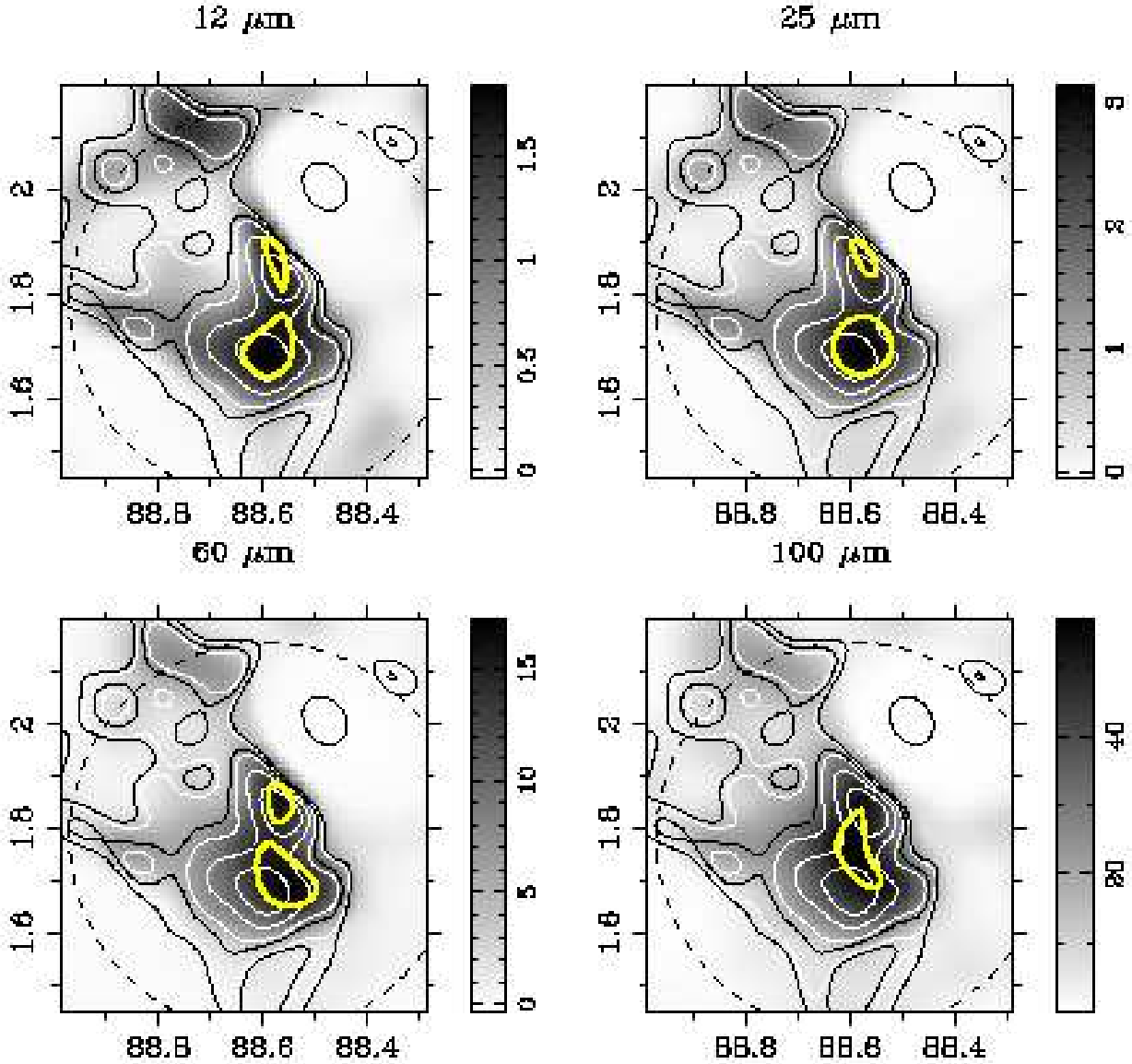


Fig. 6.— All intensity units are MJy sr^{-1} , the grey scales correspond to the MEM model for the *IRAS* templates, and the thin contours follow the CBI 31 GHz MEM model, as in Fig. 3. The thick contours follow the *IRAS* bands, at a fraction of the peak intensity: 89% for *IRAS* 12 μm , 85% for *IRAS* 25 μm and 60 μm , and 95% for *IRAS* 100 μm .

5.2.2. Statistics of the 31 GHz and IR templates correlations

In order to quantify the similarities that meet the eye when comparing the 31 GHz and the *IRAS* templates, we compute the normalised cross-correlation C of the 31 GHz MEM images with the *IRAS* models, one at a time:

$$C = \frac{\sum_i I_i(31 \text{ GHz})I_i(\text{IRAS})}{\sum_i I_i(31 \text{ GHz})^2}, \quad (1)$$

where the sums extend over all pixels in the model images. We can estimate the significance of the results by calculating the scatter of the cross-correlation C for each of 90 different realisations of noise on the template visibilities (see Appendix B).

We attempted to assign a χ^2 value to the comparison between the CBI and the *IRAS* models. But the pixels in the model images are correlated, and the covariance matrix is prohibitively large, with $\sim 170^4$ elements, in the case of 170^2 free-parameters per MEM model. The tests we ran to estimate the covariance matrix from the simulations described in Sec. 3 showed we need many more than only 90 different noise realisations. We reached a suitable accuracy on the covariance matrix only in the useless case of a model image with ~ 10 free parameters.

Table 2 lists the cross-correlation results, which are also summarised in Fig. 7. The weighted average of the 60 and 100 μm cross-correlations is worse than that of the 12 μm and 25 μm cross-correlations by 6.6σ . The solid line on Fig. 7 has a slope of $-1.84 \cdot 10^{-3} \pm 2.9 \cdot 10^{-4}$, and is thus different from zero at 6.3σ . To test the hypothesis that C is independent of *IRAS* band we calculate $\chi^2 = \sum_{j=1}^4 (C_j - \langle C \rangle)^2 / \sigma_j^2$ with the data from Table 2, where $\langle C \rangle$ is the weighted average of the cross-correlations. Reduced χ^2 is 7.7 for 3 degrees of freedom, which discards a constant value of the cross-correlation as a function of *IRAS* wavelength.

We also carried out the same simulations but with a different entropy term, S_b (described in Appendix A), obtaining the same results at lower significance. In this case the mid-IR – far-IR difference is 3.7σ , or 4.4σ after subtraction of the YSO L1622-10.

Table 2. Results from the cross-correlations in the image plane.

	12 μm	25 μm	60 μm	100 μm
<i>C</i> :	0.782 ± 0.022	0.748 ± 0.021	0.647 ± 0.015	0.624 ± 0.019

Note. — uncertainties are 1σ

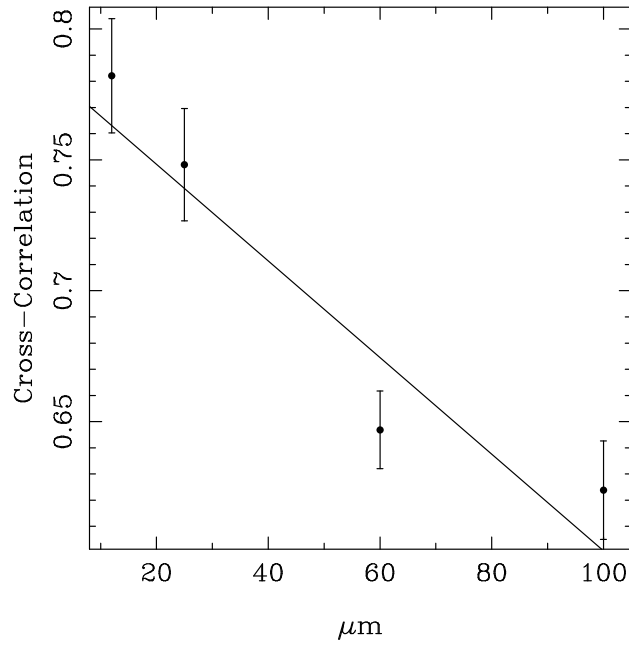


Fig. 7.— The cross-correlation of the 31 GHz and *IRAS* images (y -axis) as a function of wavelength (x -axis).

5.3. Interpretation

The comparison between the CBI image and the four *IRAS* bands allows us to conclude that the CBI emission is best represented by *IRAS* 12 μ m. The morphology of the mid-IR *IRAS* maps is suggestive of limb-brightening of a VSG-emitting shell coincident with LDN 1622’s PDR, as required by UV excitation of the VSGs.

LDN 1622 is a rather peculiar cloud in that its mid-IR emission is limb-brightened. By contrast, LDN 1591 reaches higher 100 μ m intensities than LDN 1622, and yet is not detected by Finkbeiner et al. (2002). The facts that LDN 1591 is not limb-brightened and that the 26–36 GHz emissivity is enhanced in LDN 1622 lead us to propose that the 26–36 GHz emission stems from the photon-dominated region, with abundant UV radiation. This scenario is consistent with “spinning dust”, or electric dipole radiation from spinning VSGs exposed to the incident UV radiation and charged by the photo-electric effect. A possible test for this interpretation may derive from the analysis of the cm-wave morphology of other limb-brightened clouds, such as DC300-17 in Chamaeleon (Laureijs et al. 1989), which like LDN 1622 also harbors low-mass YSOs.

Could “magnetic dipole emission” from large grains, proposed by Draine & Lazarian (1999), also account for the mid-IR – cm-wave correlation? The fact that the 100 μ m emission does not trace the 31 GHz double-peaked morphology suggests large grains, with a modified black-body spectrum, do not contribute at 31 GHz. An increased 31 GHz emissivity through a temperature enhancement in the PDR of LDN 1622 would have a concomitant limb-brightened morphology at 100 μ m. We infer a classical dust temperature map for LDN 1622, shown on Fig. 8, from the *IRAS* 60/100 μ m color map. We adopted a ν^2 emissivity law, and degraded the two maps to a common resolution guided by the point sources in the field. We solve for the dust temperature using the Brent method (Press et al. 1996), pixel by pixel. It is apparent that the large grain temperature is fairly constant across LDN 1622, and does not follow the 31 GHz contours.

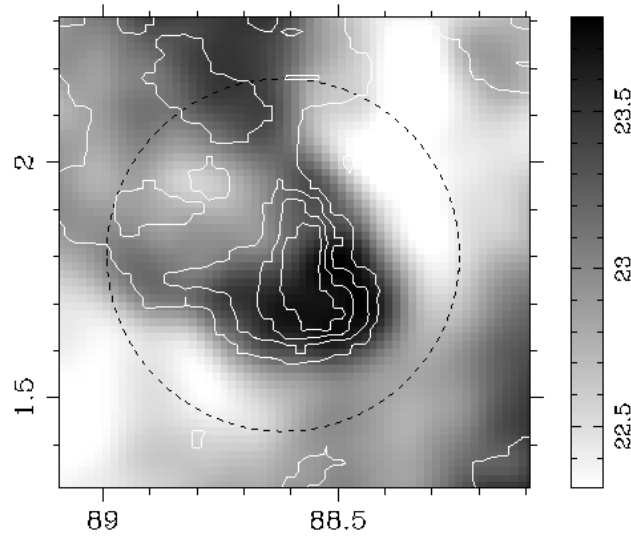


Fig. 8.— *IRAS* 60 μm contours overlaid on the dust temperature (in K) inferred from the *IRAS* 60 and 100 μm maps.

It may be argued that the *IRAS* 12 μm band is not well suited to trace VSGs because it is often contaminated by ionic line emission, for instance by [Ne II] 12.8 μm , which could arise in the PDR at the surface of LDN 1622. But the similarity of the 12 μm and 25 μm maps argue against significant line contamination. It would be very contrived to have just the right contribution of flux from lines in both bands (although the H₂ lines could still contribute to both bands in similar proportions).

6. Comparison with H α and 5 GHz templates

The surface of LDN 1622 is exposed to the interstellar UV field. Such ionised corona of LDN 1622 is conspicuous in the SHASSA image (Gaustad et al. 2001), shown on Fig. 9. The V-shaped H α corona points towards the Orion OB 1b association (Wilson et al. 2005, their Fig. 1). We note LDN 1622 corresponds to a minimum in H α brightness, therefore it is a foreground object obscuring the diffuse H α from the Orion-Eridanus bubble, consistent with the short distance of Wilson et al. (2005).

That the 31 GHz emission is not free-free is apparent from Fig. 9, where H α seems to anti-correlate with the radio continuum, although we did not attempt to correct the H α map for extinction. The H α and free-free emission both trace electron-ion collisions, so that if the electron temperature is constant, then the unreddened H α intensities are proportional to the radio-continuum specific intensities. But the only correspondence between 31 GHz and H α is at (88.15,+1.4), and stems from the outskirts of Barnard’s Loop. There is no counterpart of H α emission inside the CBI primary beam.

From the comparison with the PMN survey in Fig. 9 we further confirm free-free emission is negligible at 31 GHz. There is a hint of a radio counterpart of the H α corona, but no 5 GHz emission coexists with the 31 GHz emission.

We can further test the bremsstrahlung hypothesis for the 31 GHz emission by extrapolating the observed intensity levels to 5 GHz with a spectral index of $\alpha = -0.1$, in the optically thin approximation. The restored CBI image on Fig. 2b reaches peak intensities of 0.22 Jy beam⁻¹. Since the PMN beam is 3.7 arcmin FWHM⁷, peak 5 GHz intensities should

⁷The PMN survey is published in Jy beam⁻¹ units, but its resolution depends on whether the data were acquired with the Green Bank 300-foot dish or with the Parkes 140-foot dish. We calibrated the PMN survey with the 17 brightest point sources in a 6 deg field centered on LDN 1622, using as reference the fluxes listed by Becker et al. (1991, North 6cm catalog, also based on the PMN survey). We fitted elliptical gaussians to each point source to extract fluxes, and obtained that the beam solid angle used in the intensity units must correspond to a 3.7 arcmin FWHM PSF to reproduce the catalog fluxes. The average FWHM of the

range from $264 \text{ mJy beam}^{-1}$ for an unresolved source, to 52 mJy beam^{-1} for a uniformly extended source. The root-mean-square (rms) noise in the PMN image is $\sigma = 5.8 \text{ mJy beam}^{-1}$. The absence of the 31 GHz features from the PMN image therefore allows us to rule out free-free emission at 9σ .

In order to assess possible contamination at 31 GHz by background sources, we have overplotted on Fig. 9 the entries from the NVSS catalog (Condon et al. 1998) with flux densities greater than 10 mJy , as well as the entries from the North 6 cm database (Becker et al. 1991). Only one source may be present at 31 GHz. This is PMN J0555+0116, or NVSS J055516+011622 (J2000 RA: 05:55:16.62, Dec: +01:16:22.9), which is the source at (88.72, 1.28) in Fig. 9b, and well outside the dark cloud and the CBI primary beam.

Condon et al. (1993) explain that low spatial frequencies, on scales larger than 30 arcmin in declination, are filtered-out from the PMN survey. But the CBI-PMN comparison is not affected by this filter. The PMN filter corresponds to the very largest angular scales observed by the CBI, and LDN 1622 is a compact object of order 10 arcmin in diameter. The outskirts of Barnard’s Loop, picked up in the MEM model at (88.1, +1.4), is probably filtered-out in PMN.

elliptical gaussians is $3.78 \pm 0.56 \text{ arcmin}$, coincident with the chosen intensity units.

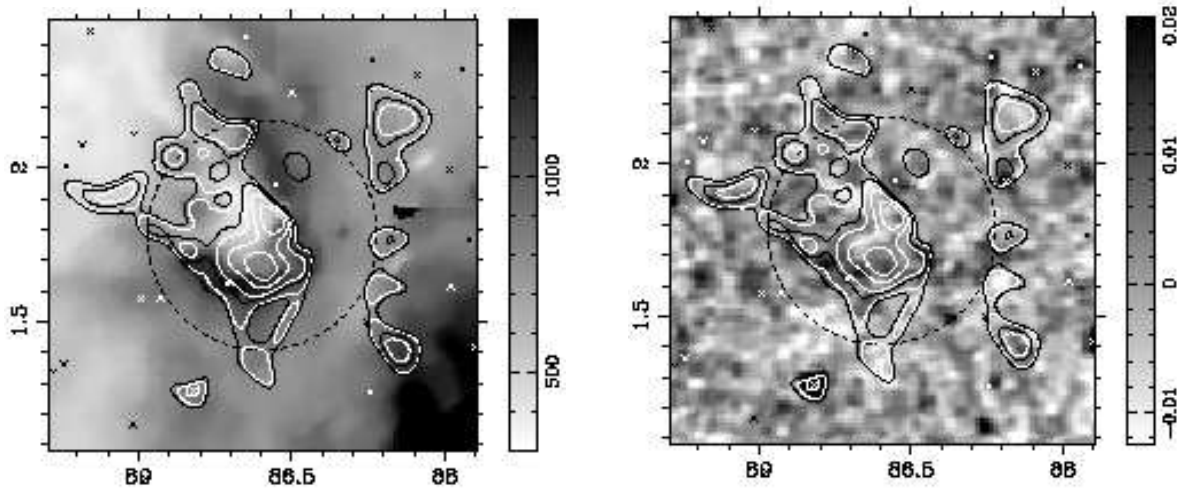


Fig. 9.— Left: 31 GHz MEM model in contours overlaid on the H α map in gray scale, with intensity units in deci-Rayleighs. Right: 31 GHz MEM model in contours overlaid on the PMN 5 GHz map, in Jy beam $^{-1}$. Crosses on both plots are the NVSS point sources, and the circle is the only point source from the North 6 cm database.

7. Spectral properties

7.1. Low-frequency spectral index

For a comparison with Finkbeiner et al. (2002) we must consider the consequences of differencing on their chopped observations, which filters-out low spatial frequencies. The flux densities in Finkbeiner et al. (2002) are referred to the *IRAS* 100 μm map by linear cross-correlation. But in general the radio and IR emissions are bound to have different power-spectra in the ISM at large. Thus in general the slopes of the straight line fits between radio and IR visibilities depend on baseline length.

In the case of LDN 1622 the radio-IR conversion factors given in Table 1 do show some variation at 12 μm when comparing cases A and B. In order to approximately account for the $\theta = 12$ arcmin chop throw of Finkbeiner et al. (2002), we restrict our analysis to baselines in excess of $\theta^{-1} \lambda$, or 286 λ , and use the non-differenced dataset. In this case, $a_{100\mu\text{m}}/10^{-3} = 0.92 \pm 0.11$, which is $\sim 2 \sigma$ higher than the value of 0.70 ± 0.01 listed in Table 1 for the full dataset.

The tentative detection of spinning dust in LDN 1622 by Finkbeiner et al. (2002) is based on a rise in flux density from 5 GHz to 9.75 GHz. Since their 5 GHz data were not chopped because of hardware limitations, the rising SED could simply reflect the missing spatial frequencies.

We nonetheless confirm the tentative detection of a rising spectrum by Finkbeiner et al. (2002): after scaling units, the value for the dimensionless $a_{100\mu\text{m}}$ at 9.75 GHz is $1.5 \cdot 10^{-4} \pm 0.5 \cdot 10^{-4}$, which by comparison with our value for $k > 286 \lambda$ implies a spectral index $\alpha_{9.75 \text{ GHz}}^{31 \text{ GHz}} = +1.57 \pm 0.31$.

7.2. CBI spectral index

Estimating a spectral index from the 10 CBI channels is difficult for an extended object such as LDN 1622 because of varying uv -coverage. Flux loss, due to missing spatial frequencies, is greater in the high-frequency channels than in the low-frequency channels.

7.2.1. Estimates from MEM models

Assuming that the MEM model is a good approximation to the sky signal, a single spectral index α can be varied to minimize

$$\chi^2 = \sum_i \|\mathbb{m}V_i(\alpha) - \mathbb{v}V_i\|^2 / \sigma_i^2, \quad (2)$$

$$\mathbb{m}V_i(\alpha) = \left(\frac{\nu_i}{\nu_o}\right)^\alpha \mathbb{m}V_i(\nu = \nu_o), \quad (3)$$

where the sum extends over all baselines and all channels. ν_o is the reference frequency used by MockCBI to scale the intensity map by the input spectral index $\alpha = 0$ to the frequency of the i^{th} visibility data point. Note that although in this application MockCBI internally uses $\alpha = 0$, the model visibilities $\mathbb{m}V_i$ still bear a frequency dependence through the uv -coverage and the primary beam. We optimize χ^2 by finding the root of $\partial\chi^2/\partial\alpha$.

The entropy term does not depend on α since it is calculated on the model image, which is kept constant for all channels in our implementation. Yet the inclusion of a regularizing entropy biases the spectral index estimates. In the case of LDN 1622, pure χ^2 reconstructions, with $\lambda = 0$, result in noisy model images, while in the absence of data a pure MEM reconstruction, with $\lambda \rightarrow \infty$, defaults to a flat image, whose intensity is M/e (see Appendix A). Increasing values of λ result in smoother model images, and the lower frequency channels recover more flux from the model images than the higher frequency channels.

We confirmed by simulation that α is recovered in pure χ^2 reconstructions. The highest value of λ for which the resulting spectral index is not significantly biased is $\lambda = 1$. To obtain this limiting value we simulated the CBI observations on template maps. We fit a model image and a single spectral index to simulated visibilities on the processed *IRAS* 12 μm and 25 μm templates. The CBI-simulated visibilities are calculated with MockCBI using $\alpha = 0$. We ran our MEM algorithm 90 times, with exactly the same settings as for the CBI models, feeding as input the CBI-simulated visibilities with the addition of 90 different realisations of Gaussian noise, as explained in Point 6 of Appendix B. We rejected models that converged early on a local minimum by requiring a minimum number of iterations N_{iter} . For reference the $\lambda = 1$ CBI model converged in $N_{\text{iter}} = 29$ iterations. The average value of best-fit indices in the simulations, without N_{iter} cutoff, is $\alpha = 0.13 \pm 0.21$ for *IRAS* 12 μm and $\alpha = 0.12 \pm 0.18$ for *IRAS* 25 μm . $\langle\alpha\rangle$ decreases with increasing N_{iter} , until it reaches the input value at $N_{\text{iter}} = 19$ for both *IRAS* 12 μm and *IRAS* 25 μm . The resulting spectral index is $\alpha = 0.009 \pm 0.172$ for *IRAS* 12 μm and $\alpha = 0.004 \pm 0.162$ for *IRAS* 25 μm , and satisfactorily close to zero, in the sense that the systematic bias due to the smoothness introduced by the entropy term is of order +0.01.

The 26–36 GHz CBI spectral index we obtained from the MEM modelling with $\lambda = 1$ is $\alpha_{\text{CBI}} = -0.38 \pm 0.13$.

7.2.2. Estimates by cross-correlation with template maps

Spectral indices are sometimes inferred by reference to a template image, as in Sec. 7.1. The 31 GHz sky image of LDN 1622 is assumed to follow exactly a template image, say *IRAS* 100 μm , so that the CBI image is a scaled version of the reference image, and $V(\nu_i) = a_i V_{\text{template}}$, where $\{\nu_i\}_{i=1}^{10}$ are the CBI channel frequencies and where V_{template} are CBI-simulated visibilities. The scaling factor a can be obtained as explained in Point 4 of Appendix B. The spectral behavior of the CBI visibilities is thus cast into the scale coefficients.

However this strategy yields inconsistent results because it is difficult to find an ideal reference image. Using the four *IRAS* band, and averaging the 10 CBI channels in two frequencies, 28.5 GHz and 33.5 GHz, we obtain spectral indices that depend strongly on the reference template and on baseline range. For the full range of baselines, α varies from $\alpha = -0.24 \pm 0.16$ for *IRAS* 12 μm to $\alpha = -0.06 \pm 0.15$ for *IRAS* 60 μm , the other *IRAS* bands giving intermediate values. For the non-differenced dataset and uv -radii in excess of 120λ , we obtain values ranging from $\alpha = -1.12 \pm 0.30$ for *IRAS* 12 μm to $\alpha = -0.75 \pm 0.31$ for *IRAS* 25 μm . All of these alternative CBI-*IRAS* cross-correlations could equally well be used to infer a spectral index. But the difference between the extremal values obtained above is greater than 3σ , and is therefore significant. These results are reported here to emphasize the systematic uncertainties involved in determinations of spectral energy distributions inferred by cross-correlations.

7.3. Integrated SED

We extracted fluxes from the *WMAP*, *IRAS*, and PMN surveys using a circular aperture with a diameter equal to the FWHM of the CBI primary beam at 31 GHz, or 45 arcmin. In order to compare with the CBI measurement, we also subtract a background level given by the flux density in the CBI reference field (offset by 8 min to the East). For all maps the reference field is essentially devoid of emission compared to the object field. To take into account flux loss, the CBI flux density we discuss here is that obtained by scaling the *IRAS* 100 μm flux density (see Sec. 4). The existing data on the integrated SED of LDN 1622 are summarised in Fig. 10 and Table 3.

Table 3. SED of LDN 1622.

ν/GHz	F_ν/Jy	
4.85	$(8.6 \pm 4.2) 10^{-2}$	PMN
5.00	$(2.1 \pm 0.4) 10^{-1}$	Green Bank ^a
8.25	$(4.1 \pm 0.8) 10^{-1}$	Green Bank ^a
9.75	$(6.2 \pm 2.1) 10^{-1}$	Green Bank ^a
23.0	2.9 ± 0.09	<i>WMAP</i>
31.0	2.9 ± 0.04	CBI ^a
33.0	2.3 ± 0.18	<i>WMAP</i>
41.0	2.0 ± 0.28	<i>WMAP</i>
61.0	2.1 ± 0.62	<i>WMAP</i>
94.0	5.4 ± 1.6	<i>WMAP</i>
3000	$(4.1 \pm 0.41) 10^3$	<i>IRAS</i>
5000	$(1.1 \pm 0.11) 10^3$	<i>IRAS</i>

Note. — ^a: measurements inferred by cross-correlation with *IRAS* 100 μm .

The spectrum of the emissivity per unit proton column density in LDN 1622 can be fit with the spinning dust emissivities of Draine & Lazarian (1998b)⁸, as first shown by Finkbeiner (2004). The data points are fit with a mixture of free-free emission, a modified blackbody representative of traditional dust emission, and the spinning dust emissivities. We require that a 15 K modified blackbody, with a 1.7 emissivity index, crosses the 90 GHz *WMAP* point⁹. The spinning dust emissivities depend on environment, and we confirm the result of Finkbeiner (2004) that the SED is best fit with a mixture of CNM and WNM emissivities (as defined by Draine & Lazarian 1998b), with a fraction of $37\pm 5\%$ CNM and $63\pm 11\%$ WNM and a proton column averaged over the CBI primary beam of $N_H = 1.24 \cdot 10^{22} \text{ cm}^{-2}$ (somewhat less than $2.4 \cdot 10^{22} \text{ cm}^{-2}$, the value used by Finkbeiner et al. (2002) referring to the peak extinction value).

The spectral indices obtained from the *WMAP* data are $\alpha_{23}^{33} = -0.62 \pm 0.23$ and $\alpha_{33}^{41} = -0.68 \pm 0.73$, or $\alpha_{23}^{41} = -0.64 \pm 0.24$, which is within 1σ from $\alpha_{\text{CBI}} = -0.38 \pm 0.13$. Combining all measurements gives a 30 GHz index $\alpha_{30 \text{ GHz}} = -0.44 \pm 0.11$.

⁸available at <http://www.astro.princeton.edu/~draine/dust/dust.mwave.html>

⁹Attempting to fit the *IRAS* 100 μm point and the *WMAP* W band simultaneously resulted in excessively low emissivity indices, or in an unrealistic sub-mm peak. The bulk of the dust in LDN 1622 is thus characterised by at least 2 modified black bodies.

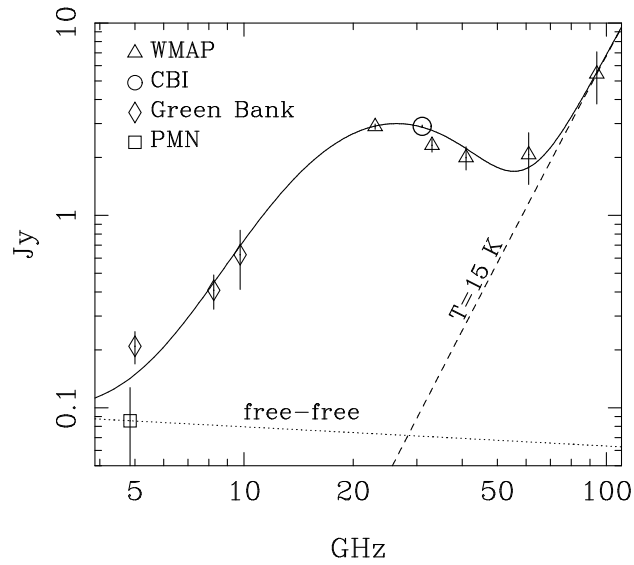


Fig. 10.— SED of LDN 1622. The solid line is a fit to the data, composed of a free-free component, a modified blackbody at 15 K with a 1.7 emissivity index representative of traditional dust emission, and the Draine & Lazarian (1998b) spinning dust emissivities.

8. Conclusions

The CBI observations of LDN 1622 resulted in the first cm-wave continuum image of a dark cloud, at frequencies where traditional emission from dust is not expected. The CBI data follow a tight correlation with the far-IR emission, confirming that the 31 GHz emission is nonetheless related to dust.

Under visual inspection the 31 GHz map is closer to the *IRAS* 12 μm and *IRAS* 25 μm maps than to the *IRAS* 100 μm map. To quantify the IR–radio similarities we calculate the cross-correlation of the 31 GHz images with each of the *IRAS* images. We find a trend for a decreasing cross-correlation with wavelength, such that the 31 GHz–12 μm comparison has the highest cross-correlation.

The mid-IR – cm-wave correlation in LDN 1622 indicates that the cm-wave continuum emission arises in a shell coincident with the PDR at the surface of LDN 1622 exposed to the Ori OB 1b UV field. The closer match between the 31 GHz and 12 μm images can be interpreted as support for spinning dust. Alternatively the 31 GHz continuum may stem from a mechanism of molecular continuum emission at 31 GHz or a dense molecular forest spread over 26–36 GHz.

We suspect the reason why the mid-IR – cm-wave correlation was not previously detected in other objects, or in the diffuse ISM, is because the *IRAS* 12 μm maps are contaminated by many more point sources than the *IRAS* 100 μm maps. The stellar emission at mid-IR wavelengths has no counterpart in cm-waves, as shown here in the case of LDN 1622.

The 10 CBI channels allow estimating a spectral index $\alpha_{\text{CBI}} = -0.38 \pm 0.13$. Combining all measurements we obtain $\alpha_{30 \text{ GHz}} = -0.44 \pm 0.11$.

This article benefitted from the constructive comments of an anonymous referee that motivated Sec. 7.3, the discussion on unresolved radiosources, Fig. 13 and its discussion in Appendix C. S.C. acknowledges support from Fondecyt grant 1030805, and from the Chilean Center for Astrophysics FONDAF 15010003. We gratefully acknowledge the generous support of Maxine and Ronald Linde, Cecil and Sally Drinkward, Barbara and Stanely Rawn, Jr., Fred Kavli, and Rochus Vogt. This work is supported by the National Science Foundation under grant AST 00-98734. We acknowledge the use of NASA’s *SkyView* facility (<http://skyview.gsfc.nasa.gov>) located at NASA Goddard Space Flight Center.

A. MEM algorithm

The MEM algorithm was programmed by us and fits model visibilities, calculated on a model image, to the observed visibilities. The free-parameters of our MEM model are the pixels in the model 170×170 image, $\{I(x_i, y_i)\}_{i=1}^{170 \times 170}$. We set to zero all pixels that fall outside a region of the sky where the expected noise is larger than a specified value. In practice, for one pointing as is the case here, this means restricting the number of free pixels to those that fall within a user-supplied radius from the phase center.

The relatively small number of visibilities for the CBI (~ 1000 for each on-off cycle) allows one to work in the uv -plane and fit for the observed visibilities directly, rather than work in the sky plane and deconvolve the synthesized beam. We did not apply any gridding of the visibilities (Briggs et al. 1999), which we postpone to a future development of our code. The use of a direct fourier transform in our current implementation is time consuming.

The model functional we minimize is $L = \chi^2 - \lambda S$, with

$$\chi^2 = \sum_i \|\text{m}V_i - \text{o}V_i\|^2 / \sigma_i^2, \quad (\text{A1})$$

where the symbol $\|z\|$ stands for the modulus of a complex number z , the sum extends over all visibilities (i.e., the sum runs over 10 channels and 78 baselines), σ_i is the root-mean-square (rms) noise on the corresponding visibility, $\text{o}V_i$ stands for the observed visibilities, and the model visibilities $\text{m}V_i$ are given by

$$\text{m}V(u_i, v_i) = \int_{-\infty}^{+\infty} A_\nu(x, y) I_\nu(x, y) \exp[-2\pi i(u_i x + v_i y)] \frac{dx dy}{\sqrt{1 - x^2 - y^2}}, \quad (\text{A2})$$

where $A_\nu(x, y)$ is the CBI primary beam and x and y are the direction cosines relative to the phase center in two orthogonal directions on the sky. The model visibilities are calculated using the MockCBI program (see below). We assume a flat spectral index for the model image, i.e. $I_\nu = I(31 \text{ GHz})$ over the 10 CBI channels.

We use the entropy $S = -\sum_i I_i \log(I_i/M)$, where $\{I_i\}_{i=1}^N$ is the model image and M is a small intensity value taken as the noise estimated by difmap and divided by 10000. We also investigated an entropy term of the form $S_b = -\sum_i \log I_i/F$, where $F = \sum_i I_i$, obtaining essentially the same results.

Image positivity is enforced by clipping. All intensities below the threshold value of M are set equal to M . Our choice for the image entropy is such that the entropy term minimizes the need for clipping with a diverging derivative at zero intensities. However we caution that the true sky signal in our differenced observations may not be strictly positive: sources in the reference field act as negative signal.

The entropy is used as a regularizing term. Because the reconstruction is degenerate in the sense that we have more free parameters than data points, pure χ^2 reconstructions lead to artificially low values of reduced χ^2 , so that χ^2 models end up fitting the noise (i.e. the residual image is artificially flat at the locus of free parameters). The parameter λ was adjusted by hand and kept fixed during the optimization. Intermediate values of λ from infinity to zero recover the sum of object signal and noise in gradually increasing detail. The exact value of λ is set by trial and error, requiring that χ^2 (Eq. A1) is close to its expected value given by approximately twice the number of imaginary data visibilities. A dimensionless value of $\lambda = 5$ ($\lambda = 5 \cdot 10^{-9}$ for S_b) gave good results when reconstructing on test images (see Fig. 11 below). We obtain a reduced χ^2 value of 1.04 for the CBI visibilities, with 25726 data points (i.e. twice the number of complex data points). Reduced χ^2 for the MEM models of the template *IRAS* images is 0.99. The slightly larger χ^2 for the CBI data is probably due to faint sources in the reference field acting as negative sky signal. The positivity requirement precludes modelling such negative signal.

Convergence is achieved in ~ 20 iterations using the Fletcher-Reeves conjugate-gradient algorithm from *Numerical Recipes* (Press et al. 1996, NR), or ~ 80 if using the *Gnu Scientific Library* (GSL, <http://www.gnu.org/software/gsl/>). The GSL algorithm is double-precision, but is too slow for our needs as it requires more gradient evaluations per iteration than in NR. Thus the models presented in this work use the NR implementation. One reconstruction takes about 30 min using the AMD Athlon XP3000 processor, or 1h with an Intel Pentium 4 at 2.80 GHz.

B. Model validation

To validate our MEM model we reconstructed the sky emission from model visibilities, obtained by a simulation of CBI observations on reference images (“CBI-simulated visibilities”). Simulation of the CBI observations is performed with the MockCBI program (Pearson 2000, private communication), which calculates the visibilities $V(u, v)$ on the input images $I_\nu(x, y)$ with the same uv sampling as a reference visibility dataset (Eq. A2). Thus MockCBI creates the visibility dataset that would have been obtained had the sky emission followed the template.

We used as reference images the maps of LDN 1622 in the four *IRAS* bands, as downloaded from *SkyView* (<http://skyview.gsfc.nasa.gov>). The procedure is as follows:

1. Subtract conspicuous mid-IR point-sources in the $12 \mu\text{m}$ and $25 \mu\text{m}$ 3×3 degree fields. We fit elliptical gaussians on a second order polynomial surface. Only one of these

point-sources coincides with the object itself, namely L1622-10 (see Appendix C), but all contribute to the simulated visibilities. L1622-10 is an entry in the *IRAS* Point Source Catalog, so it was removed from the $12\mu\text{m}$ template by subtracting a point source with L1622-10’s tabulated $12\mu\text{m}$ flux of 1.027 Jy, with a PSF given by the minimum width of the elliptical gaussian fits to the other point sources (5.4 arcmin FWHM). We performed tests both with and without subtraction of L1622-10.

2. Clip the *IRAS* images so that the minimum intensity value is zero. The processed images are shown on Fig. 11.
3. Simulate CBI visibilities on the processed *IRAS* images using MockCBI.
4. Cross-correlate the observed CBI visibilities with the model visibilities to obtain 31 GHz–far-IR conversion factors, a : $V(31\text{ GHz}) = aV(\text{IRAS})$, in the complex plane. We fit for a by minimising $\chi^2 = \sum_i \|V(31\text{ GHz}) - aV(\text{IRAS})\|^2/\sigma_i^2$, where the notation is the same as in Eq. A1.
5. Divide the model visibilities by a to obtain model visibilities scaled to the 31 GHz values. Values for a are given in Table 1, for case A (differenced dataset).
6. Add gaussian noise to the complex model visibilities, (i.e. we assume the model visibilities have no noise), with a dispersion given by the root-mean-square (rms) noise on the corresponding CBI visibility.
7. Run the MEM reconstruction algorithm with the same parameters as for the observed CBI data.
8. Repeat the simulation 90 times with 90 different realisations of noise.
9. Average the 90 model images. We tested that the measured scatter in the properties of the simulated reconstructions does not increase when increasing the number of noise realisations from 60 to 90 (although 30 realisations was not enough).

We did not take into account the finite resolution of the *IRAS* maps, which is due to the coarse pixelization used in the *IRAS* Sky Survey Atlas maps available at *SkyView*. The net effect is that the template resolution is lower than that of the CBI data. The mid-IR point sources allow estimating that the natural-weight synthesized beam is 20% larger for the *IRAS* simulations than for the CBI data.

Fig. 11 shows the average MEM models overlaid on the input maps, and allows judging by inspection the level of detail that can be recovered from the CBI visibilities of LDN 1622. In this case we used the full uv -coverage of the CBI, as in Fig. 2.

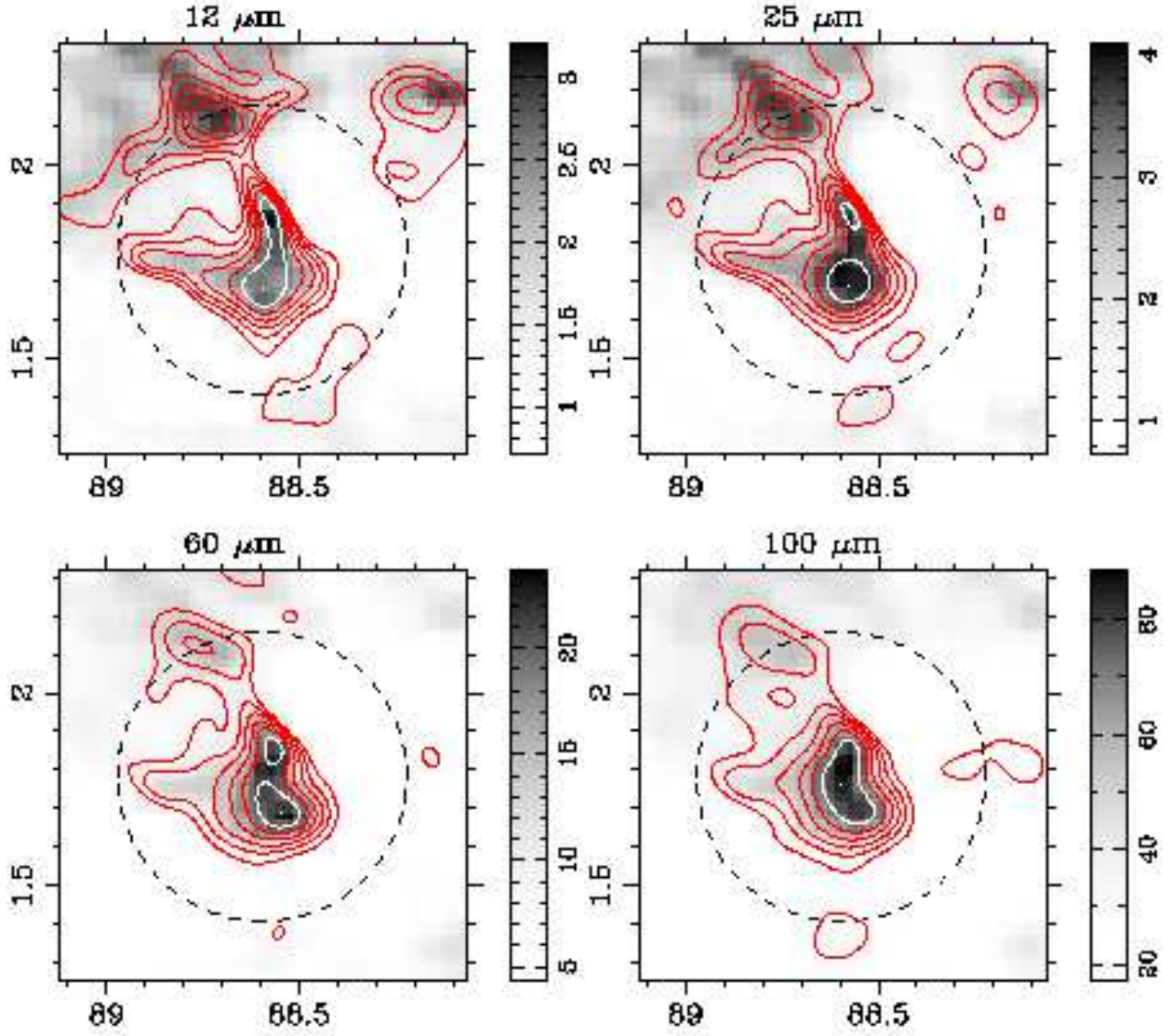


Fig. 11.— Input *IRAS* template maps in grey scale, with overlays of our average MEM reconstructions from CBI-simulated data and 90 different realisations of gaussian noise. The x and y axis are J2000 R.A. and Dec, in degrees of arc. Flux units are MJy sr^{-1} .

C. Mid-IR point sources

Although LDN 1622 figures in lists of starless cores (Lee et al. 2001; Park et al. 2004) it harbors an entry of the *IRAS* Point Source Catalog¹⁰, IRAS 05517+0151, whose presence can be inferred from the *IRAS* 12 μ m image in Fig. 11, because the peak of emission at a position of (88.58, 1.87) is bright and unresolved, and stands out over the diffuse emission. IRAS 05517+0151 is coincident within the uncertainties with an entry from the 2MASS catalog (Cutri et al. 2003), 2MASS 05542277+0152039, and with the binary pre-main-sequence star L1622-10 (J2000 RA: 05:54:26.8, Dec: +01:52:16, Reipurth & Zinnecker 1993).

The YSO is very clear as a saturated pixel in the ISOCAM¹¹ 6.7 μ m image of LDN 1622 presented by Bacmann et al. (2000). Note that LDN 1622 is curiously listed as LDN 1672 in Bacmann et al. (2000), and the orientation of the image is not as that obtained from the *ISO* archive, and is thus probably wrong. For these reasons we present in Fig. 12 an overlay of the *IRAS* 12 μ m emission in contours on the upright ISOCAM 6.7 μ m map. The 12 μ m peak and the saturated region at 6.7 μ m are coincident.

¹⁰Infrared Astronomical Satellite Catalogs, 1988. The Point Source Catalog, version 2.0, NASA RP-1190

¹¹ISO is an ESA project with instruments funded by ESA Member States (especially the PI countries: France, Germany, the Netherlands and the United Kingdom) and with the participation of ISAS and NASA. The ISO TDT and AOT codes for the image used here are 69802905 and C01, and the observer is P. André.

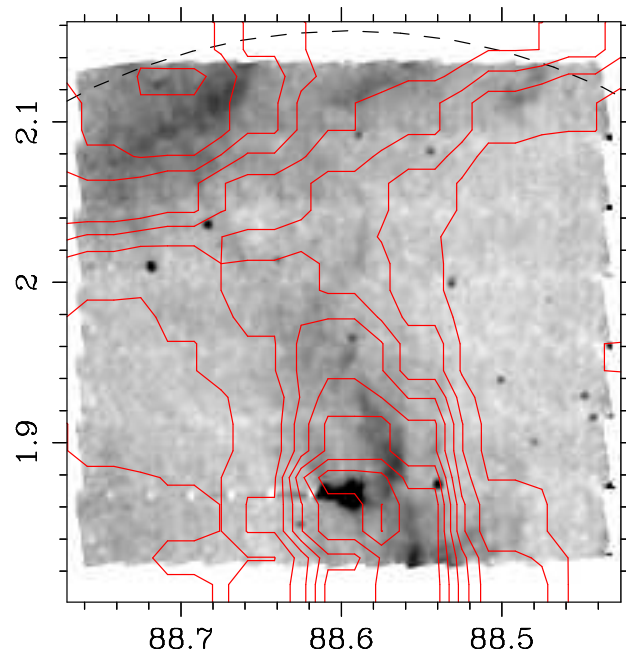


Fig. 12.— The *IRAS* 12 μm contours overlaid on the 6.7 μm ISOCAM mosaic of LDN 1622 in grey scale (arbitrary units), highlighting the presence of a YSO at (88.58, 1.87). The dashed arc traces the FWHM of the CBI primary beam. The x and y axis are J2000 R.A. and Dec, in degrees of arc.

L1622-10 is probably a T-Tauri binary (Reipurth & Zinnecker 1993). We extracted the B, R, and I, photometry of L1622-10 from the USNO-B10 Catalog (Monet et al. 2003), and constructed the SED shown on Fig. 13. An estimate of the ISO flux is included at $6.7 \mu\text{m}$, but is assigned zero weights because the presence of pixel glitches spreading away from L1622-10 suggests the detector may be saturated. The *IRAS* $25 \mu\text{m}$ flux is also assigned zero weight because of uncertainties in the nebular contamination. A simple blackbody fit gives a temperature of $1680 \pm 50 \text{ K}$, using conservative uncertainties on the data points, and a linear size of $0.2 \pm 0.01 \text{ AU}$ for a distance of 120 pc. The integrated luminosity of the blackbody fit is thus $2.8 L_{\odot}$, corresponding to a $1.4 M_{\odot}$ main-sequence star, which confirms that the YSO is a low-mass object.

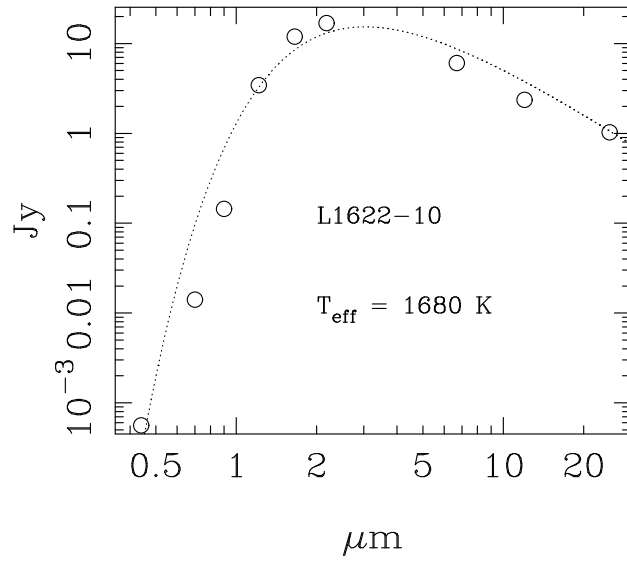


Fig. 13.— The spectral energy distribution of the most conspicuous YSO coincident with LDN 1622. The dotted line is a blackbody fit to the data points, shown in circles.

REFERENCES

- Bacmann, A., André, P., Puget, J.-L., Abergel, A., Bontemps, S., Ward-Thompson, D., 2000, *A&A*, 361, 555
- Banday, A.J., Dickinson, C., Davies, R.D., Davis, R.J., Górski, K.M., 2003, *MNRAS*, 345, 897
- Becker, R. H., White, R. L., Edwards, A. L. 1991, *ApJS*, 75, 1
- Bevington, P.R., Robinson, D.K., 1992, in “Data Reduction and Error Analysis for the Physical Sciences”, 2nd edition, McGraw-Hill
- Boumis, P., Dickinson, C., Meaburn, J., Goudis, C. D., Christopoulou, P. E., López, J. A., Bryce, M., Redman, M. P., 2001, *MNRAS*, 320, 61
- Briggs, A.S., Schwab, F.R., Sramek, R.A., 1999, in “Synthesis Imaging in Radio Astronomy II”, *ASP Conference Series* 180, 127
- Casassus, S., Readhead, A.C.S., Pearson, T.J., Nyman, L.Å., Shepherd, M.C., Bronfman, L., 2004, *ApJ*, 603, 599
- Condon, J. J., Cotton, W. D., Greisen, E. W., Yin, Q. F., Perley, R. A., Taylor, G. B., Broderick, J. J., 1998, *AJ*, 115, 1693
- Condon, J.J., Griffith, M.R. & Wright, A.E., 1993, *AJ*, 106, 1095
- Cutri, R.M., et al., 2003, “The 2MASS All-Sky Catalog of Point Sources”, University of Massachusetts and Infrared Processing and Analysis Center (IPAC/California Institute of Technology).
- de Oliveira-Costa, A, Tegmark, M., Finkbeiner, D.P., Davies, R.D., Gutierrez, C.M., Haffner, L.M., Jones, A.W., Lasenby, A.N., Rebolo, R., Reynolds, R.J., Tufte, S.L., Watson, R.A., 2002, *ApJ*, 567, 363
- de Oliveira-Costa, A., Tegmark, M., Gutiérrez, C.M., Jones, A.W., Davies, R.D., Lasenby, A.N., Rebolo, R., Watson, R.A., 1999, *ApJ*, 527, 9
- Désert, F.-X., Boulanger, F., Puget, J.L., 1990, *A&A*, 237, 215
- Draine, B.T., Lazarian, A., 1998, *ApJ*, 494, L19
- Draine, B.T., Lazarian, A., 1998, *ApJ*, 508, 157

- Draine, B.T., Lazarian, A., 1999, ApJ, 512, 740
- Draine, B.T., Li, A., 2001, ApJ, 551, 807
- Elmegreen, B. G., 2002, ApJ, 564, 773
- Finkbeiner, D.P., 2004, ApJ, 614, 186,
- Finkbeiner, D.P., Davis, M., Schlegel, D.J., 1999, ApJ, 524, 867
- Finkbeiner, D.P., Schlegel, D.J., Frank, C., Heiles, C., 2002, ApJ, 566, 898
- Gaustad, J.E., McCullough, P.R., Rosing, W., Van Buren, D., 2001, PASP, 113, 1326
- Gautier, T.N. III, Boulanger, F., Péroult, M., Puget, J.L., 1992, AJ, 103, 1313
- Heiles, C., Haffner, L.M., Reynolds, R.J., Tufte, S.L., 2000, ApJ, 536, 335
- Li, A., Draine, B.T., 2001, ApJ, 554, 778
- Lagache, G., 2003, A&A, 405, 813
- Laureijs, R.J., Chlewicki, G., Wesselius, P.R., Clark, F. O., 1989, A&A, 220, 226
- Lee, C.W., Myers, P. C., Tafalla, M., 2001, ApJS, 136, 703
- Lee, C.W., Myers, P. C., 1999, ApJS, 123, 233
- Leitch, E.M., Readhead, A.C.S., Pearson, T.J., Myers, S.T., 1997, ApJ486, L23
- Lynds, B.T., 1962, ApJS, 7, 1
- Maddalena, R.J., Morris, M., Moscowitz, Thaddeus, P., 1986, ApJ, 303, 375
- Monet D.G., Levine S.E., Casian B., et al., 2003, AJ, 125, 984.
- Padin, S., et al, 2002, PASP, 114, 83
- Page, L., Nolta, M. R., Barnes, C., Bennett, C. L., Halpern, M., Hinshaw, G., Jarosik, N., Kogut, A., Limon, M., Meyer, S. S., Peiris, H. V., Spergel, D. N., Tucker, G. S., Wollack, E., Wright, E. L., 2003, ApJS, 148, 39.
- Park, Y.-S., Lee, C. W., Myers, P. C., 2004, ApJS, 152, 81

- Pearson, T. J., Mason, B. S., Readhead, A. C. S., Shepherd, M. C., Sievers, J. L., Udomprasert, P. S., Cartwright, J. K., Farmer, A. J., Padin, S., Myers, S. T., Bond, J. R., Contaldi, C. R., Pen, U.-L., Prunet, S., Pogosyan, D., Carlstrom, J. E., Kovac, J., Leitch, E. M., Pryke, C., Halverson, N. W., Holzzapfel, W. L., Altamirano, P., Bronfman, L., Casassus, S., May, J., Joy, M., 2003, *ApJ*, 591, 556
- Press, W.H., Flannery, B.P., Teukilsky, S.A., Vetterling, W., Y., 1996, *Numerical Recipes* (Cambridge, Cambridge University Press)
- Reipurth, B., Zinnecker, H., 1993, *A&A*, 278, 81
- Shepherd, M.C., 1997, in *Astronomical Data Analysis Software and Systems VI*, ed. G Hunt & H.E. Payne, ASP conference series, v125, 77-84 “Difmap: an interactive program for synthesis imaging”.
- Van Dishoeck, E.F., 2004, *ARA&A*, 42, 119
- Watson, R. A., Rebolo, R., Rubiño-Martín, J. A., Hildebrandt, S., Gutiérrez, C. M., Fernández-Cerezo, S., Hoyland, R. J., Battistelli, E. S., 2005, *ApJ*, 624, 89
- Wheelock, S., et al., 1991, *IRAS Sky Survey Atlas Explanatory Supplement*
- Wilson, B.A., Dame, T.M., Mashedier, M.R., Thaddeus, P., 2005, *A&A*, 430, 523
- Wright, E.L., 1998, *ApJ*, 496, 1